X-1 Experiment Chamber Design and Analysis: Progress Report for the Period August 1, 1998 to September 30, 1998

R.R. Peterson, G.L. Kulcinski, E.A. Mogahed,
H.Y. Khater, M.E. Sawan, I.N. Sviatoslavsky,
P. Cousseau, J.F. Santarius, K. Olson, T. Utschig,
D.L. Henderson, M.L. Corradini, R.L. Engelstad, G.A. Moses

October 1998

UWFDM-1094

FUSION TECHNOLOGY INSTITUTE

UNIVERSITY OF WISCONSIN

MADISON WISCONSIN

X-1 Experiment Chamber Design and Analysis:
Progress Report for the Period
August 1, 1998 to September 30, 1998

R.R. Peterson, G.L. Kulcinski, E.A. Mogahed, H.Y. Khater, M.E. Sawan,
I.N. Sviatoslavsky, P. Cousseau, J.F. Santarius, K. Olson, T. Utschig,
D.L. Henderson, M.L. Corradini, R.L. Engelstad, G.A. Moses

Fusion Technology Institute
Department of Engineering Physics
University of Wisconsin-Madison
1500 Engineering Drive
Madison, WI 53706

October 1998

UWFDM-1094

Table of Contents

1. Executive Summary

The preliminary analysis of the X-1 experiment chamber has been conducted and several issues have been identified for further work. The X-1 experiment chamber will experience a considerably harsher environment than does the NIF chamber. Even in the case of experiments where there is no thermonuclear yield from the target, the energy in the X-1 chamber is conservatively estimated to be 20 MJ in magnetic debris and 16 MJ in x-rays. If a thermonuclear target yield of 200 MJ is achieved, another 60 MJ of target debris and x-rays and 140 MJ of neutrons are added. Without thermonuclear yield in a NIF target only 1 MJ of x-rays, 0.8 MJ of debris, plus reflected or unabsorbed laser light will be produced. An ignited target NIF would add about 3 MJ in x-rays and 1 MJ of debris. Because the NIF target chamber was designed to be just below the vaporization threshold and is quite large (5.5 m radius), the much larger energies in X-1 make it practically impossible to avoid substantial vaporization and melting in the experiment chamber. The fusion neutrons from yield shots and, to a lesser degree, photoneutrons and ions will activate the experiment chamber. The challenge of the X-1 design activity is to develop an experiment chamber concept that allows radioactive vapor, molten material and shrapnel to be contained in a way that allows for maintenance and timely operation of the facility.

The experimental chamber concept is depicted in Figure 1. The design employs a "defense in depth" strategy. Multiple layers of protection are used to confine the blast generated by the energy contained in the chamber. The first level of protection is the hemispherical mini-chamber made of Kevlar with a graphite inner coating, which it meant to stop the large pieces of magnetic debris, and most of the x rays and debris ions emitted by the target. The mini-chamber may need replacement after shots with a burning ICF capsule, but it will be designed not to become a debris source itself. The next layer is an aluminum liner that will absorb those x-rays and debris ions that pass through holes in the mini-chamber. Both the liner and the mini-chamber will experience significant vaporization and melting. After a shot, the liner can be removed as a unit with the radioactive rubble trapped in inside. Fast-closing explosive valves will prevent radioactive debris from leaving the experiment chamber. Outside, the liner is an aluminum structural wall designed to carry the impulsive and long-term pressure loading from the blast. Outside of that is a water shield to stop fusion neutrons and gamma rays emitted by radioactive materials.

This experiment chamber concept is flexible with respect to its pulsed power interface. There are at least two types of pulsed power options for X-1. One has many long coaxial magnetically insulated transmission lines (MITLs) that converge on the equatorial waist of the cylindrical experiment chamber. These MITLs can traverse space of almost any type: air, water, or solid shield. In this experiment chamber concept, the MITLs are first surrounded by air for many meters, then traverse through 2.5 m of water before joining the experiment chamber. Several individual MITLs are connected by a few conical MITLs inside the experiment chamber. Magnetic insulation is continuous across the experiment chamber wall. Therefore, no insulator stack is required.

In the other main type of pulsed power, a very thick water tank surrounds the chamber, which contains many water transformers. This concept also uses conical MITLs inside the chamber, but since the magnetic insulation begins at the chamber wall, an insulator stack is required. The only major difference between the experiment chambers for the two pulsed power concepts is the

presence of a plastic insulator stack. The survival issues for this insulator stack are discussed herein. It is clear that a failure of the stack would allow the mixing of a large volume of tritiated water with the radioactive rubble inside the chamber and must be avoided at all cost.

The experiment chamber design must also be flexible in its use. At the recent workshop on Applications of Pulsed Power to Stockpile Stewardship in Las Vegas, Nevada, many experiments to study radiation effects, equation-of-state, opacity, fluid instabilities, mix, and radiation flow were suggested for X-1. These experiments could be performed using both ignited targets and no yield shots. The expected yield for these experiments could have a wider energy range than has yet been studied for the X-1 experiment chamber. Also, the relative energies in debris, x-rays and neutrons will vary among these experiment types. Diagnostic access will also vary. Radiation effects experiments will require large test samples with debris mitigation and large x-ray scattering structures. The current design can be adapted to accommodate these experiments.

The University of Wisconsin has performed preliminary analysis of some aspects of this experiment chamber concept. These include the target-generated blast, the mechanical response of the experiment chamber to these blasts, and neutronics and radioactivity. The analysis assumes that the target x-ray, debris ion and neutron emissions have the same spectra as in the LIBRA-SP target, but that the energy release is scaled to 200 MJ of yield. Target emission calculations for an X-1 target concept are in progress, but are not yet used in the experiment chamber response analysis. The target x-rays and debris ions vaporize significant amounts of material from the mini-chamber, 0.247 kg for 200 MJ yield and 0.142 kg for the no thermonuclear yield case. The vaporization imparts a large recoil impulse to the chamber wall and mini-chamber, which could lead to mechanical failure. The mini-chamber receives impulses of 136 and 67 Pa-s with or without thermonuclear yield, while the chamber wall liner impulse is 41.2 or 18.4 Pa-s. Mechanical analysis has been performed for the wall liner, but not the mini-chamber. There is confidence that vessels can be designed to withstand such impulses. The biological dose rate has been calculated for 200 MJ yield shots, and it has been found that the chamber concept allows access to the back of the water shield a few hours after a shot and hands-on access to the chamber wall 10 days after the shot. For no thermonuclear yield, access is allowed through the experiment chamber several hours after a shot.

A number of critical issues remain for the X-1 experimental chamber. They should be addressed during the conceptual design of X-1 as well as throughout the construction and operation of X-1. These include the following:

- Remote maintenance and removal of an experimental chamber after a yield shot and minimization of facility downtime.
- X-ray, debris, and neutron output from all likely experiments.
- Production of secondary debris by interaction of the target emissions with the target support structures and power feeds.
- Exact determination of impurities present in chamber materials, including structures and diagnostics and calculation of radioactivity and biological dose rates due to these impurities.
- Fragmentation of mini-chamber, cryogenic equipment, and diagnostics into damaging shrapnel and the effects that shrapnel might have on the experimental chamber.

- Migration of radioactive rubble into diagnostic and pulsed power ports and the design of fast closing valves.
- Effect of diagnostics and pulsed power ports and conical MITLs on the dynamics of the experimental chamber.
- Verification of all computer codes used in the experiment chamber design through experiments.

2. Neutronics and Activation

2.1 Activation Analysis

The neutron flux obtained from the neutron transport calculations is used in the activation calculations. The calculations are performed using the computer code DKR-PULSAR[1] with the FENDL-2[2] activation cross section library. The neutron transmutation data used is in a 46-group structure format. The gamma source data is in 21-group structure format. The calculations are performed assuming one year of operation. Using the DKR-PULSAR code allows for appropriate modeling of the pulse sequence in ICF chambers. In a previous analysis of the Laboratory Microfusion Facility[3], it was shown that assuming an equivalent steady state operation (where the flux level is reduced to conserve fluence) results in underestimating the dose rates at shutdown by several orders of magnitude. The underestimation becomes negligible within a week after shutdown. The large underestimation within a short period of time following shutdown is due to the fact that the activity during this time is dominated by short-lived radionuclides. The activities of short-lived isotopes are usually sensitive to the operational schedule prior to shutdown due to their buildup during the ontime with subsequent decay during the dwell time. On the other hand, the long-term activity is dominated by long-lived radionuclides whose activity is determined by the total neutron fluence regardless of the temporal variation of the flux level.

The calculations are performed for three different types of shots. The first are radiation shots with a pulsing schedule of 1 shot per day for a total of 240 shots per year. Only photoneutrons are produced during these shots. The second types of shots considered are moderate yield shots. These shots produce a neutron yield of 200 MJ and have a pulsing schedule of 2 shots per month for a total of 24 shots per year. The third type of shots considered are high yield shots. These shots also use a pulsing schedule of 2 shots per month for a total of 24 shots per year resulting in a neutron yield of 1000 MJ.

The decay gamma source produced by the DKR-PULSAR code is used to calculate the biological dose rate after shots at different locations inside and outside the water tank. The DKR-PULSAR code gives the decay gamma source at different times following shutdown. The adjoint dose field is then determined by performing a gamma adjoint calculation using the ONEDANT code with the flux-to-dose conversion factors representing the source at the point where the dose is calculated. The decay gamma source and the adjoint dose field are then combined to determine the biological dose rate at different times following shutdown. In addition, the specific activities calculated by the DKR-PULSAR code for the different radionuclides are used to evaluate the radwaste classification of the chamber wall as well as the MITL structure according to both the NRC 10CFR61[4] and Fetter[5] waste disposal concentration limits.

2.2 Biological Dose Rates

Biological dose rates are calculated at six different locations for different times following shots. These locations are shown in Figure 1. The two alloys Al-5083 and 2 1/4 Cr-1 Mo steel are considered as chamber material candidates. Figure 2 shows a comparison between the biological dose rates expected outside the chamber and inside the water tank at all times following shots for the two alloys. Using the aluminum chamber allows for hands-on maintenance ten days following moderate yield shots. On the other hand, using the steel chamber would not allow for hands-on maintenance at all times following shots. In this analysis, the limits for hands-on maintenance were assumed to be around 2.5 mrem/hr. In the case with aluminum alloy in the chamber wall, the dose rates within the first few minutes following shots are dominated by the decay of ^{24m}Na ($T_{1/2}$ = 20.2 ms) produced from ^{27}Al (n, γ) reaction. During the first few hours, the doses are dominated by ^{24}Na ($T_{1/2}$ = 14.96 hr) produced from ^{23}Na (n, γ), ^{24}Mg (n, p), and ^{27}Al (n, γ) reactions and ^{27}Mg ($T_{1/2}$ = 9.45 min) produced from ^{26}Mg (n, γ), ^{27}Al (n, p), and ^{30}Si (n, γ) reactions. The dose rates during the first week continue to be dominated by the decay of ^{24}Na. ^{54}Mn ($T_{1/2}$ = 312.2 d) is the dominant nuclide in the period up to ten years following shots. At times beyond 10 years after shutdown, the dose rates are caused by the decay of the ^{26}Al ($T_{1/2}$ = 7.3 x 10^5 yr). ^{26}Al is produced via the ^{27}Al (n, 2n) reaction.

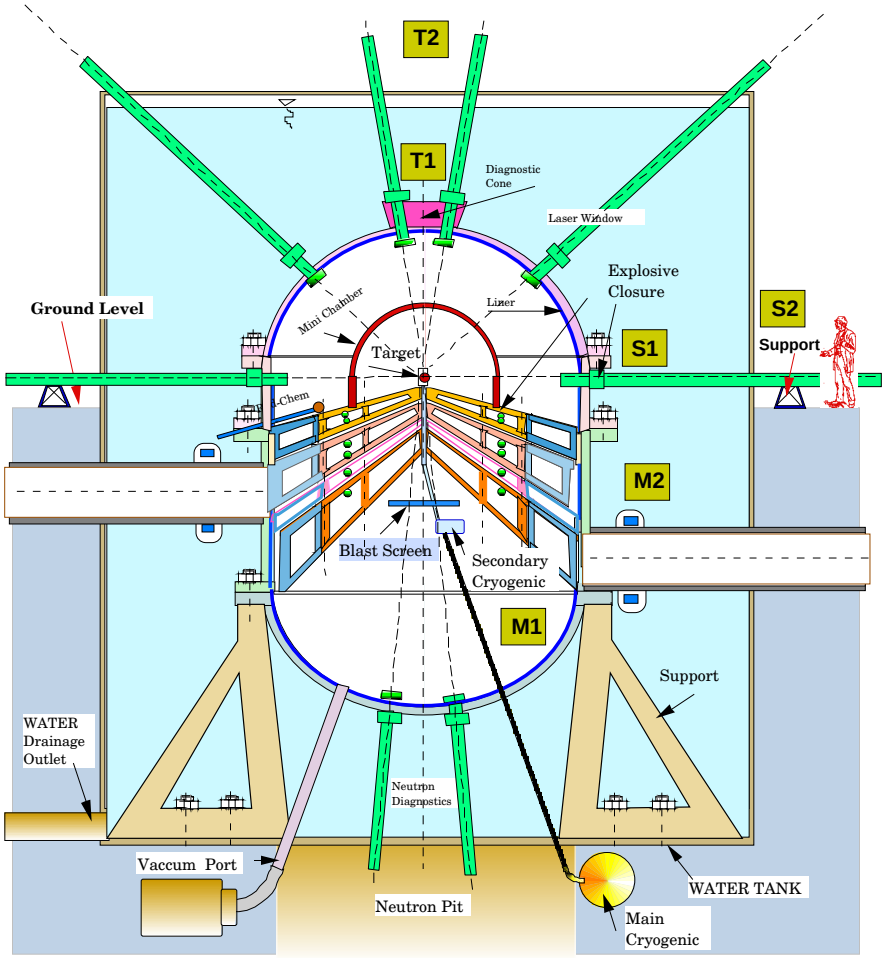

Figure 1. Locations at which dose rates are calculated.

In the case of the 2 1/4 Cr-1 Mo steel chamber, the dose rate during the first few minutes following shots is dominated by ^{28}Al and ^{52}V ($T_{1/2}$ = 3.76 min) produced from ^{51}V (n, γ), ^{52}Cr (n, p), and ^{55}Mn (n, γ) reactions. The high content of manganese in the steel chamber results in ^{56}Mn ($T_{1/2}$ = 2.578 hr) being the major contributor to the dose rate up to one day. Even though most of the ^{56}Mn is produced as a result of the ^{55}Mn (n, γ) reaction, a significant amount is also produced by the ^{56}Fe (n, p) reaction. In the period between 1 day and 10 years, as in the case of the aluminum chamber, ^{54}Mn and ^{60}Co dominate the dose rate produced in the steel chamber. Beyond ten years after shots, the dose rate is primarily dominated by radionuclides induced from the steel impurities. The two major contributors are ^{94}Nb ($T_{1/2}$ = 2 x 10^4 yr) produced from ^{93}Nb (n, γ) and ^{94}Mo (n, p), and ^{93}Mo ($T_{1/2}$ = 3,500 yr) produced from ^{92}Mo (n, γ) and ^{94}Mo (n, 2n) reactions.

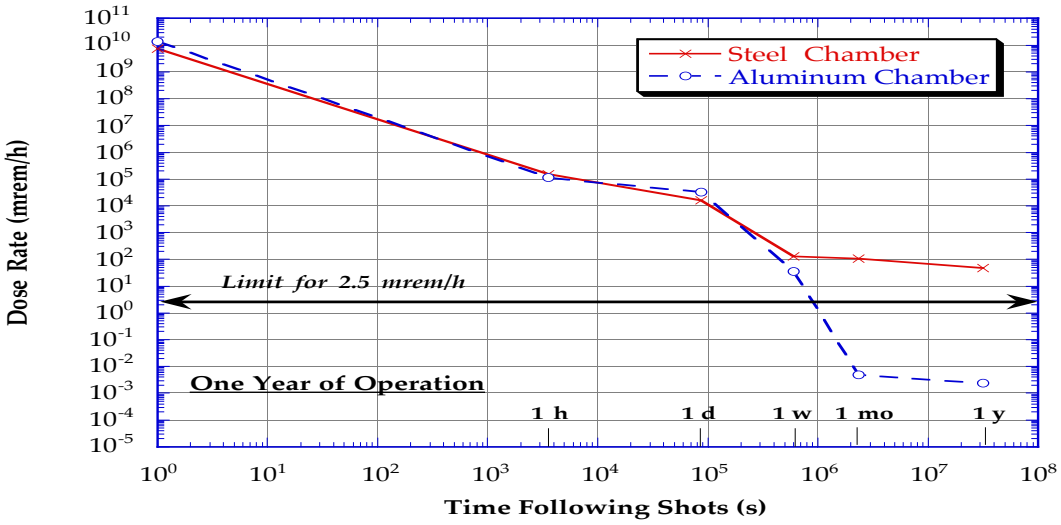

Figure 2. Biological dose rates at location "T1" following moderate yield shots.

The issue of keeping water in the tank vs. draining it during maintenance and the possibility of using borated water instead of regular water are examined. As shown in Figure 3, draining water from the tank will have no impact on the dose rates inside the tank as in such a case the dose is dominated by the contribution from the chamber wall. Figure 4 shows that replacing water in the tank with borated water did not have much of an effect on the dose rate beyond the first minute following shots. During the first minute following a shot, gammas from the decay of ^{16}N ($T_{1/2}$ = 7.13 s) contribute significantly to the total dose. ^{16}N is produced in water via the ^{16}O (n, p) reaction. The presence of boron, with its high neutron absorption cross section, in the borated water results in significant reduction in the amount of ^{16}N generated in the tank. However, boron absorption of neutrons results in the production of a large amount of tritium. We decided that the high tritium inventory as well as the extra cost associated with the use of boron made it a non-attractive alternative to water. Figure 4 also shows that the are outside the tank could be accessed following moderate shots much faster if water is kept in the tank. Keeping water in the tank helps in reducing the dose exposure from the chamber wall and limits the dose to

maintenance personnel to doses from irradiated equipment outside the tank. In this analysis, the equipment is represented by a 50 cm thick layer of copper located a meter away from the tank surface. As shown in Figures 5 and 6, doses to the side of the tank are similar to those expected at the top of the tank (Figures 3 and 4). However, as shown in Figure 7, locations in the lower part of the tank are better shielded due to the presence of the MITL resulting in faster access to these locations following shots. Figure 8 shows that no hands-on maintenance could be allowed inside the chamber following moderate or high yield shots.

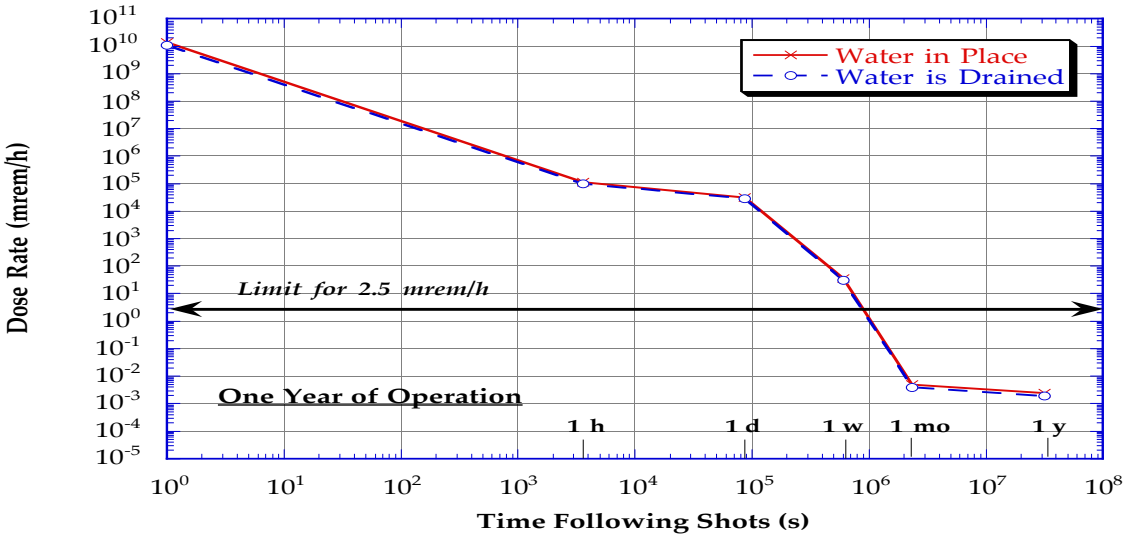

Figure 3. Impact of draining water on biological dose rates at location "T1" following moderate yield shots.

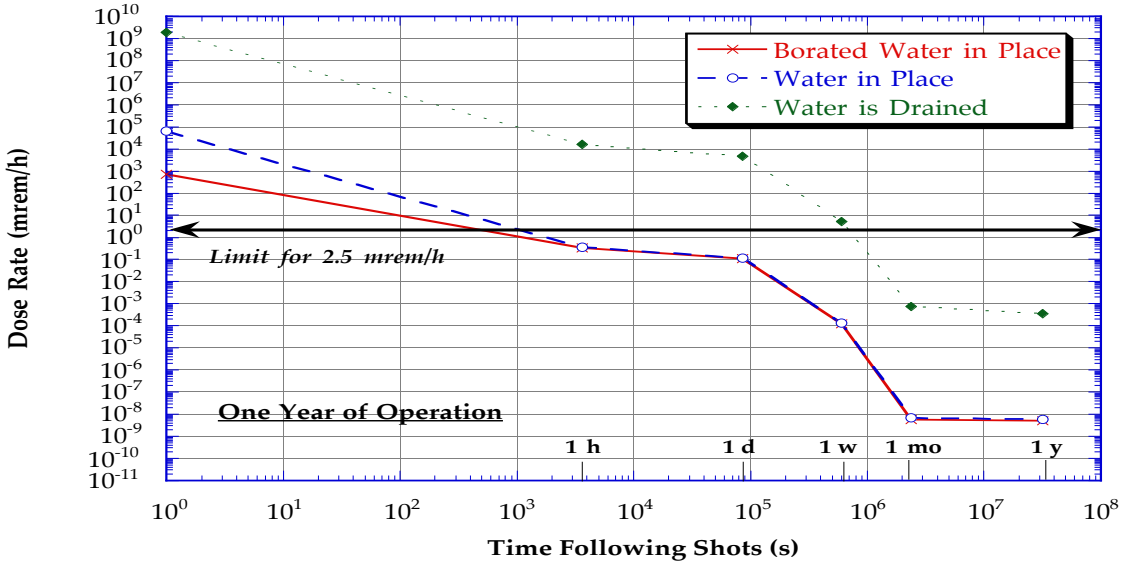

Figure 4. Impact of using borated water on biological dose rates at location "T2" following moderate yield shots.

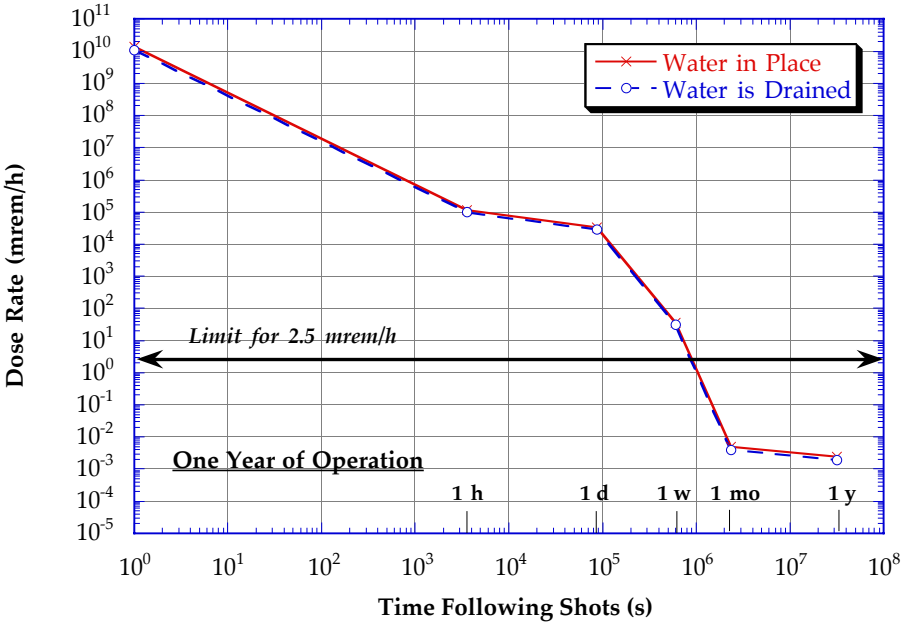

Figure 5. Biological dose rates at location "S1" following moderate yield shots.

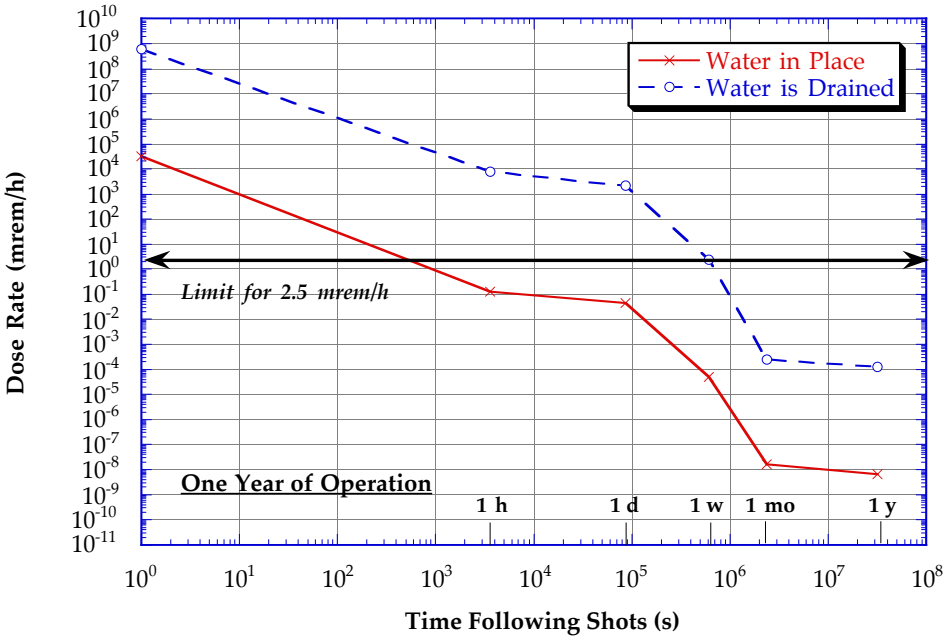

Figure 6. Biological dose rates at location "S2" following moderate yield shots.

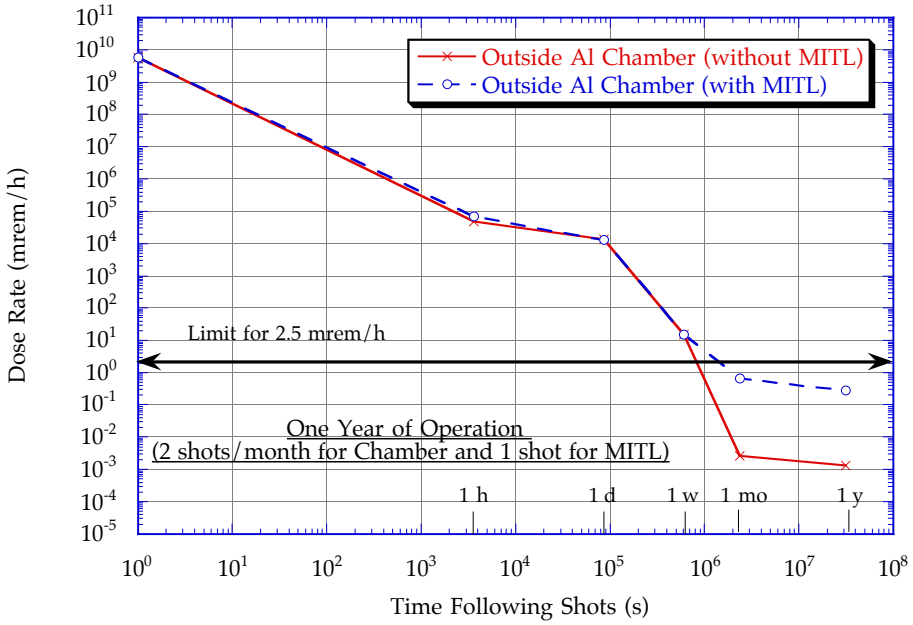

Figure 7. Biological dose rates at location "M2" following moderate yield shots.

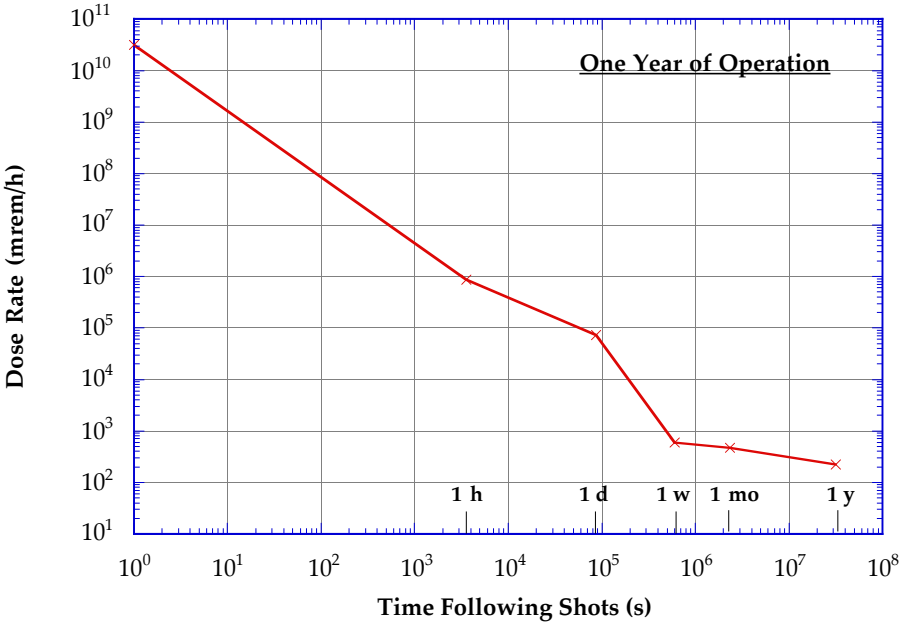

Figure 8. Biological dose rates inside the chamber (at location "M1") following moderate yield shots.

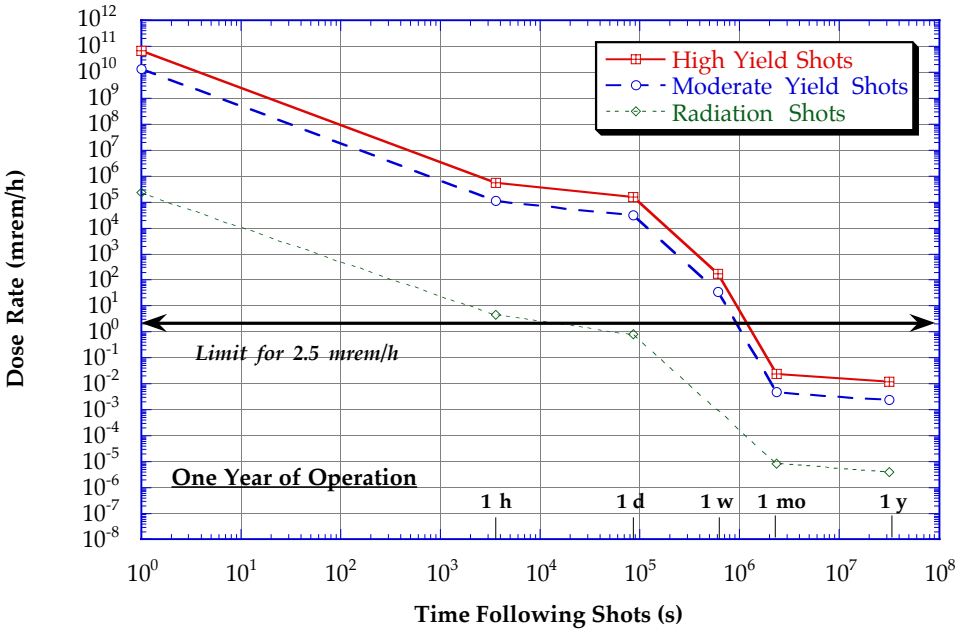

Figure 9. Biological dose rates at location "T1" following all types of shots.

During radiation shots, much smaller levels of dose are caused by the photoneutrons produced as a result of the interaction between the Bremsstrahlung radiation and the inner MITL materials. This analysis assumed a total Bremsstrahlung photon production of 5.62×10^{18} photon per shot. The photons are assumed to be monoenergetic with peak energy of 18 MeV. Using a conservative average iron (n, γ) cross section of 5 mb led to the production of 9.56×10^{15} neutrons in the inner MITL. The neutrons had an average energy of 7 MeV. The photoneutron source is used in the neutron transport calculation to calculate the flux for the activation and dose calculations. Figure 9 shows a comparison between the dose rates inside the tank following the three different type of shots considered in this analysis. Dose rates behind the chamber following radiation shots are four orders of magnitude lower than dose rates following moderate yield shots. In the mean time, dose rates following high yield shots are a factor of five higher than dose rates following moderate yield shots. As shown in Figure 10, hands-on maintenance activities outside the chamber may be allowed few hours following radiation shots. A waiting period of more than a day is needed before accessing the inside of the chamber following radiation shots.

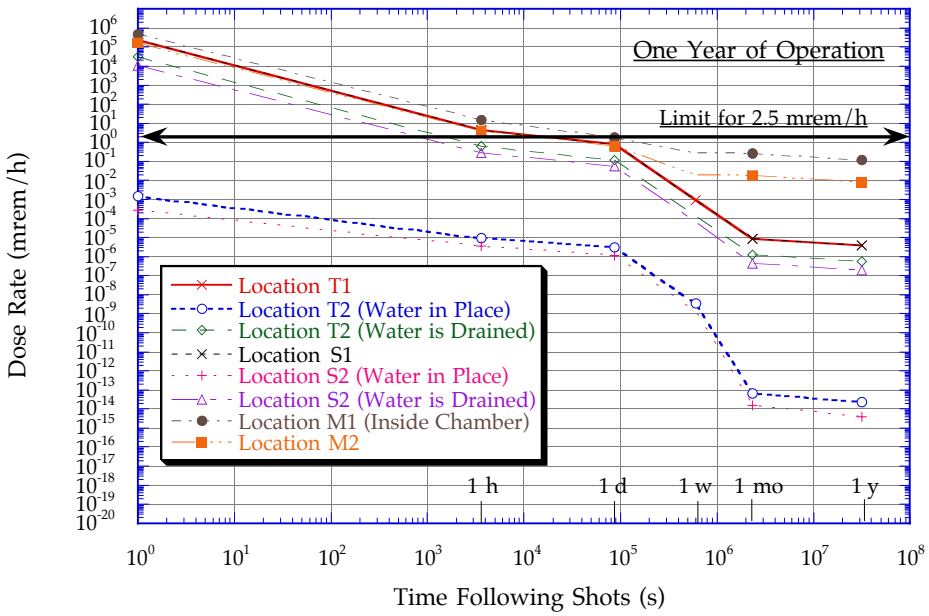

Figure 10. Biological dose rates at all locations following radiation shots.

2.3 Water Activation

Activation of water present in the tank results in the production of a large amount of ^{16}N and a much smaller amount of tritium. Figures 11 and 12 show the radial variation of the production of ^{16}N and tritium, respectively. ^{16}N has a very short lifetime of 7.13 seconds during which it produces high-energy gammas (6.13 and 7.12 MeV). However, due to the very short lifetime, the dose caused by the ^{16}N gamma decay drops significantly within the first few minutes following shots. On the other hand, tritium is more of a concern from a safety point of view. Assuming that the total amount of water in the tank is about 480 tonnes and the average rate of tritium production in the water tank is 0.0374 μCi/m^3, the total inventory of tritium in the water tank is about 18 μCi. To estimate the potential hazard associated with such a low level of tritium in the water tank, off-site early doses are estimated using the rem/Ci values calculated using the MACCS2 code[6]. The off-site dose calculations are performed using the following (worst release) conditions:

- Ground release.
- Atmospheric stability class F.
- 1 km site boundary.
- 1 m/s wind speed.

Since tritium could also be released in the form of HTO, the calculations showed that the off-site early dose inventories for tritium and HTO are 1.43 and 158.2 prem, respectively.

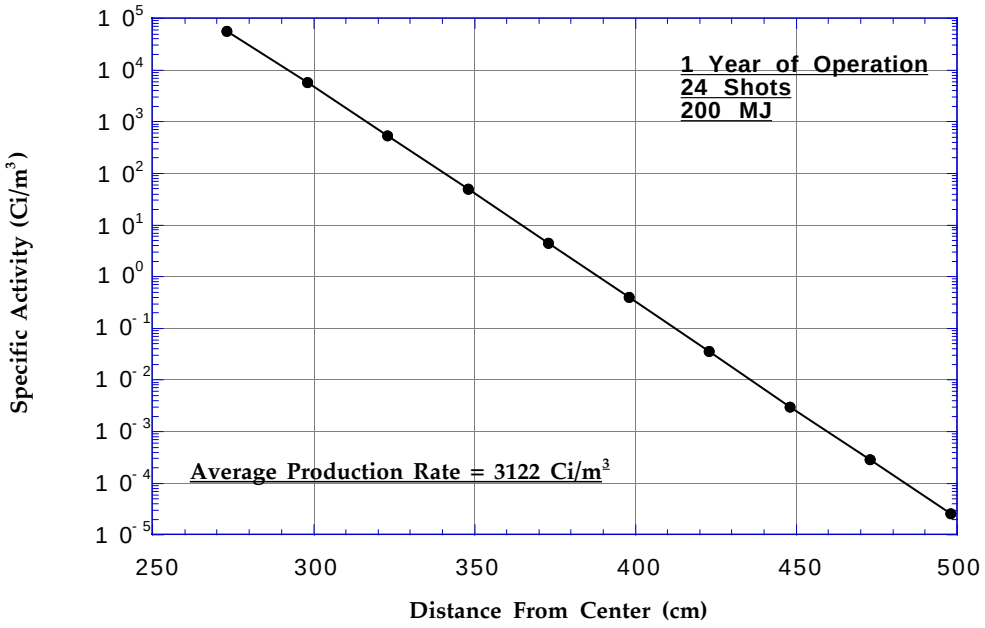

Figure 11. Radial distribution of ^{16}N generated in the water tank.

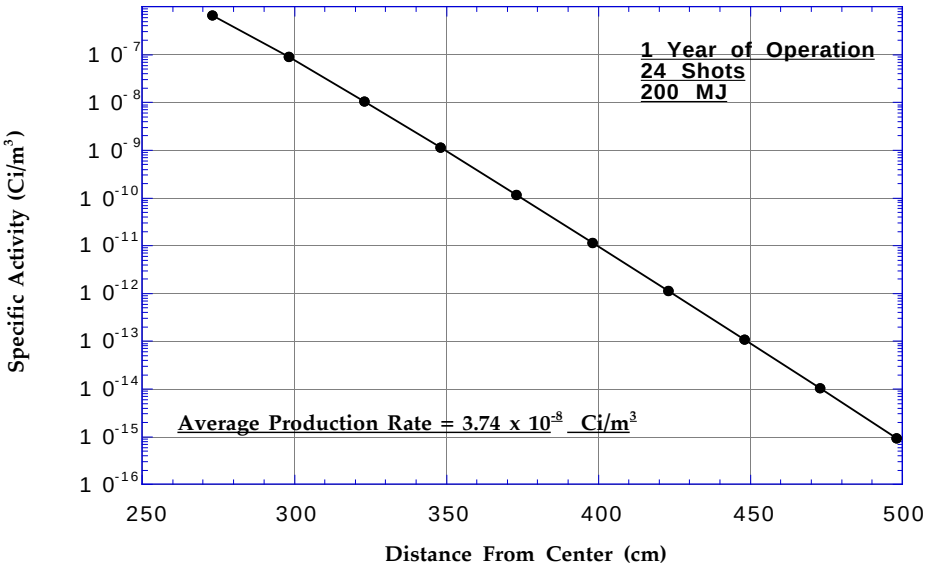

Figure 12. Radial distribution of tritium generated in the water tank.

2.4 Waste Disposal Ratings

The waste disposal ratings are evaluated according to both the NRC 10CFR61 and Fetter waste disposal concentration limits. The 10CFR61 regulations assume that the waste disposal site will be under administrative control for 100 years. The dose at the site to an inadvertent intruder after the 100 years is limited to less than 500 mrem/year. The waste disposal rating (WDR) is defined as the sum of the ratio of the concentration of a particular isotope to the maximum allowed concentration of that isotope taken over all isotopes and for a particular class. If the calculated WDR ≤ 1 when Class A limits are used, the radwaste should qualify for Class A segregated waste. The major hazard of this class of waste is to individuals who are responsible for handling it. Such waste is not considered to be a hazard following the loss of institutional control of the disposal site. If the WDR is > 1 when Class A WDL are used but ≤ 1 when Class C limits are used, the waste is termed Class C intruder waste. It must be packaged and buried such that it will not pose a hazard to an inadvertent intruder after the 100-year institutional period is over. Class C waste is assumed to be stable for 500 years. Using Class C limits, a WDR > 1 implies that the radwaste does not qualify for shallow land burial. Fetter developed a modified version of the NRC's intruder model to calculate waste disposal limits for a wider range of long-lived radionuclides which are of interest for fusion researchers than the few that currently exist in the current 10CFR61 regulations. Fetter's model included more accurate transfer coefficients and dose conversion factors. However, while the NRC model limits the whole body dose to 500 mrem or the dose to any single organ (one of seven body organs) to 1.5 rem, Fetter limits are based on the maximum dose to the whole body only. The specific activities calculated for the different radionuclides have been used to evaluate the radwaste classification of the chamber and MITL structure. Table 1 shows the waste disposal ratings for each of the type of shots considered. As shown in the table, the chamber and MITL will qualify for disposal as Class C low-level waste according to both limits.

Table 1. Waste Disposal Ratings.

Zone	Limits	Shots	WDR	Dominant Nuclides
Chamber	10CFR61	Moderate Yield	4.4e-12	^{14}C
Chamber	10CFR61	Radiation	6.1e-15	^{14}C
Chamber	Fetter	Moderate Yield	8e-6	^{26}Al
Chamber	Fetter	Radiation	1.2e-14	^{10}Be
MITL	10CFR61	Moderate Yield	1.5e-6	^{94}Nb
MITL	10CFR61	Radiation	1.8e-10	^{94}Nb
MITL	Fetter	Moderate Yield	4.9e-6	^{26}Al
MITL	Fetter	Radiation	1.5e-10	^{94}Nb

2.5 Future Neutronics and Activation Work

- Response of insulator stack to large instantaneous dose rates.
- Target neutronics with the appropriate X-1 target configuration.
- Multi-dimensional neutronics and shielding calculations for the chamber.
- Assessment of streaming into chamber penetrations.
- Multi-dimensional activation and dose calculations.
- Biological dose rate calculations following radiation shots using actual Bremsstrahlung spectrum.
- Charged particle activation using actual proton spectrum.
- Detailed waste stream analysis.

References for Section 2

1. J. Sisolak, Q. Wang, H. Khater and D. Henderson, "DKR-PULSAR2.0: A Radioactivity Calculation Code that Includes Pulsed/Intermittent Operation," to be published.

2. A. Pashchenko et al., "FENDL/A-2.0: Neutron Activation Cross-Section Data Library for Fusion Applications," Report INDC (NDS)-173, IAEA Nuclear Data Section, March 1997.

3. H. Y. Khater and M. E. Sawan, "Dose Rate Calculations for a Light Ion Beam Fusion Laboratory Microfusion Facility," Proc. IEEE Thirteenth Symposium on Fusion Engineering, Knoxville, TN (October 1989) 1412-1415.

4. Nuclear Regulatory Commission, 10CFR part 61, "Licensing Requirements for Land Disposal of Radioactive Waste," Federal Register, FR 47, 57446 (1982).

5. S. Fetter, E. Cheng and F. Mann, "Long Term Radioactive Waste from Fusion Reactors," Fusion Engineering and Design, Vol. 13, pp. 239-246 (1990).

6. M. L. Abbott, S. L. Harms, and A. S. Rood, "Dose Calculations for Accidental Airborne Releases of ITER Activation Products," Idaho National Engineering Laboratory Report, EGG-EEL-10994 (1993).

3. Mechanical Response

3.1 Mini-Chamber

After a 200 MJ target explosion, the X-1 mini-chamber experiences an impulse of 136 Pa-s, a peak pressure of 6.2 Mbar, and a residual pressure of 4.3 MPa. This is the loading due to x-ray and ion driven ablation of the graphite coating. In addition to this, there is magnetic debris consisting of large chunks of high velocity metal. The mechanical response to the combined loading is under consideration at this time. The magnetic debris has average energy fluence more than half of the x-ray fluence and it is concentrated in large pieces. Whereas the ablation loading will be smoothly varying over the inner surface of the mini-chamber, the magnetic debris will form countable numbers of craters. Many of these craters will penetrate the graphite liner into the Kevlar backing.

The mini-chamber will respond to both loadings by shock propagation from the surface and the craters and vibration. Kevlar was chosen as a material to minimize fracture due to shocks and vibration. It is expected that the mini-chamber may require replacement after each high yield shot, but that it will not become a debris source in itself. Detailed analysis of the response needs to be done, including 3-D finite element analysis of the vibrations and 2-D dynamic analysis of the crater formation and shock propagation.

3.2 Chamber

A full 360° 3-D model of the experiment chamber without any of the internal components (for example the MITLs) was developed. This model was created in the finite element package ANSYS using shell elements (8 noded). The purpose of the model is to study the dynamic response of the experiment chamber to an impulsive pressure. Also, this model can be used to determine the non-axisymmetric natural frequencies of the experiment chamber. These frequencies could be excited by ambient vibrations; for example, rotating machinery like vacuum pumps. Two views of the solid model of the perforated experiment chamber created in ANSYS are shown in Figures 13 and 14. The coordinate triad shows the location of the target inside the chamber.

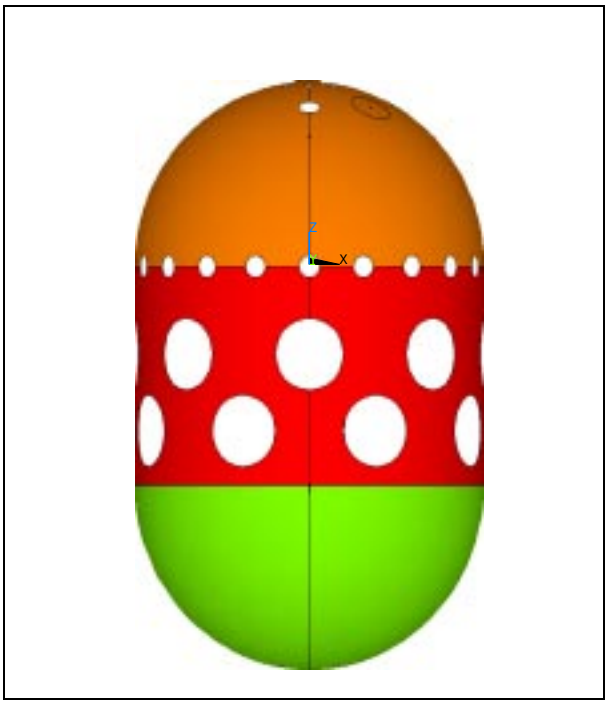

Figure 13. Front view of the solid model of the experimental chamber.

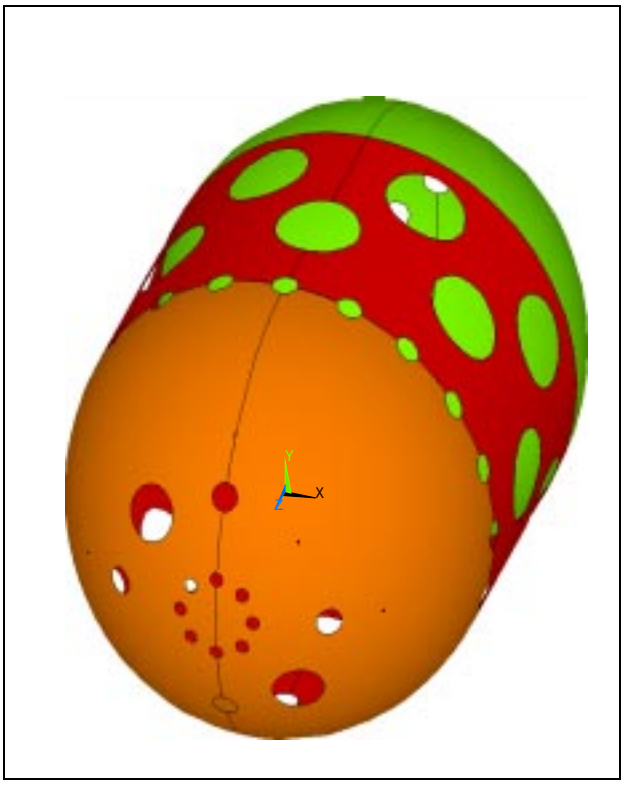

Figure 14. Isoparametric view of the solid model of the experimental chamber.

3.3 MITL

To study the combined response of the MITLs and the chamber wall, an axisymmetric finite element mode was developed in ANSYS, shown in Figure 15. The axisymmetric model is rotated about the y-axis to create the full 360° model. Since the model is axisymmetric, no perforations in the chamber wall are present. The MITLs were modeled by a homogeneous cone. The base of the cone is rigidly attached to the side of the chamber wall and a hole is present at the apex of the cone to leave a gap for the target. The coordinate triad in Figure 15 indicates the location of the target in the chamber. The experiment chamber's flange support is approximated by a pinned boundary condition, which prevents displacement but allows rotation. For the transient analysis, a uniform impulsive pressure is applied to the top hemisphere and to the top of the MITLs that is represented by the arrows in Figure 15. Even thought the axisymmetric model is basic, it does a good job of predicting the response of the structure and can be used to benchmark more complex models, for example the model shown in Figures 13 and 14.

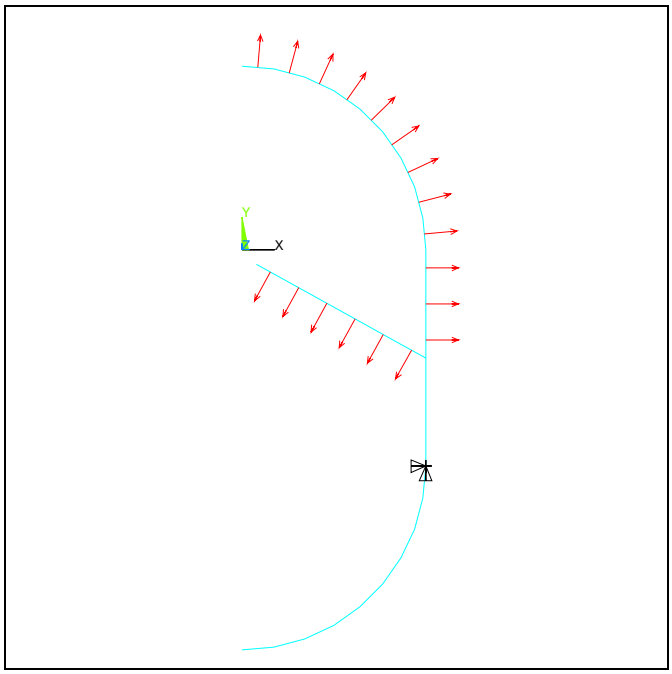

Figure 15. Axisymmetric model of the MITL and target chamber.

A modal analysis of the axisymmetric structure was performed. Figure 16 shows the lowest three non-torsional mode shapes. The motion of the MITLs dominates the mode at 129 Hz. Movement of the top hemisphere of the experimental chamber dominates the 199 Hz mode and the bottom hemisphere deforms the greatest in the 244 Hz mode. In addition, the fundamental torsional mode (not shown) was located between the 129 Hz and the 199 Hz mode.

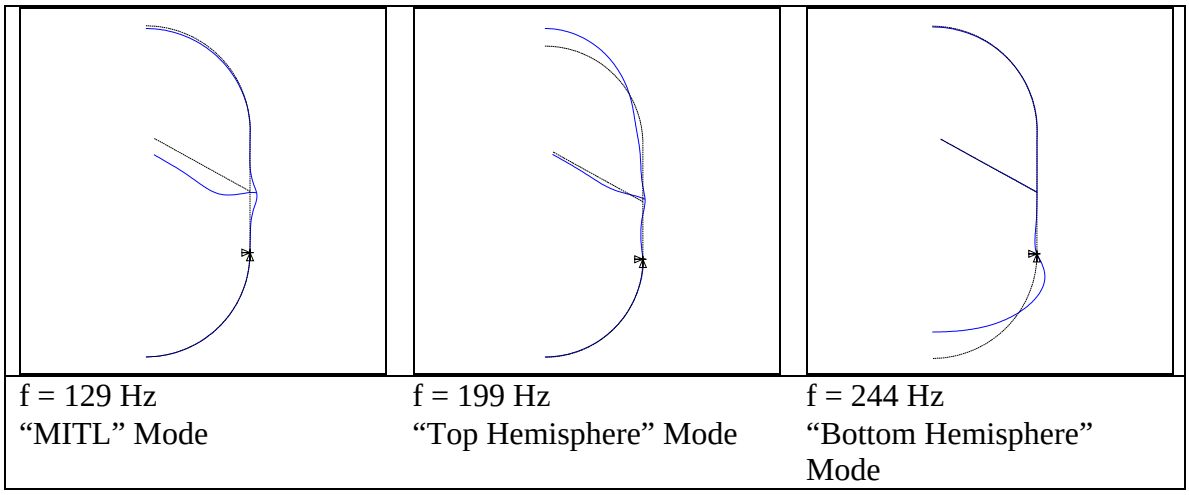

f = 129 Hz “MITL” Mode	f = 199 Hz “Top Hemisphere” Mode	f = 244 Hz “Bottom Hemisphere” Mode

Figure 16. Axisymmetric natural frequencies of the experiment chamber.

A transient analysis of the axisymmetric model was performed. A uniform impulsive pressure of 40 Pa-s (200 MJ target yield) was applied to the top hemisphere and to the top of the MITLs. The radial deflection as a function of time at the junction of the MITLs and the chamber wall from the impulse is shown in Figure 17. The hoop stress at the junction of the MITLs and the chamber wall is shown in Figure 18.

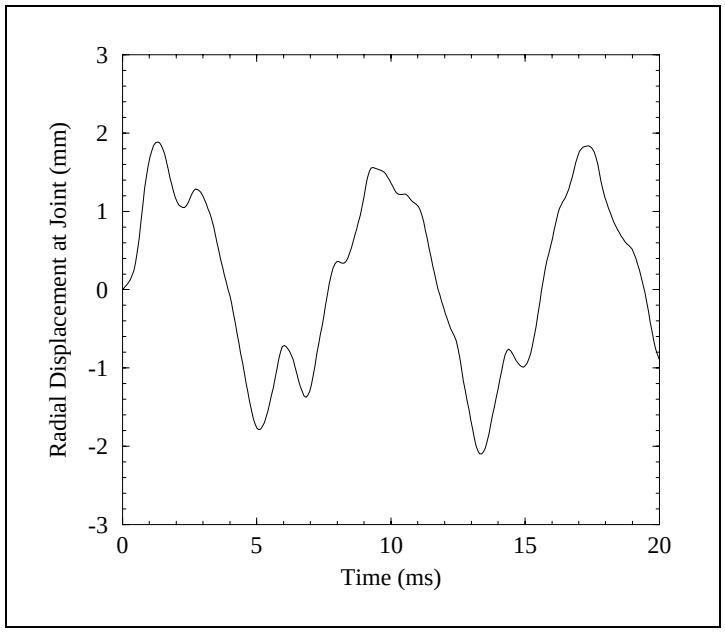

Figure 17. Radial deflection at the junction of the MITLs and the chamber wall from a 40 Pa-s impulse.

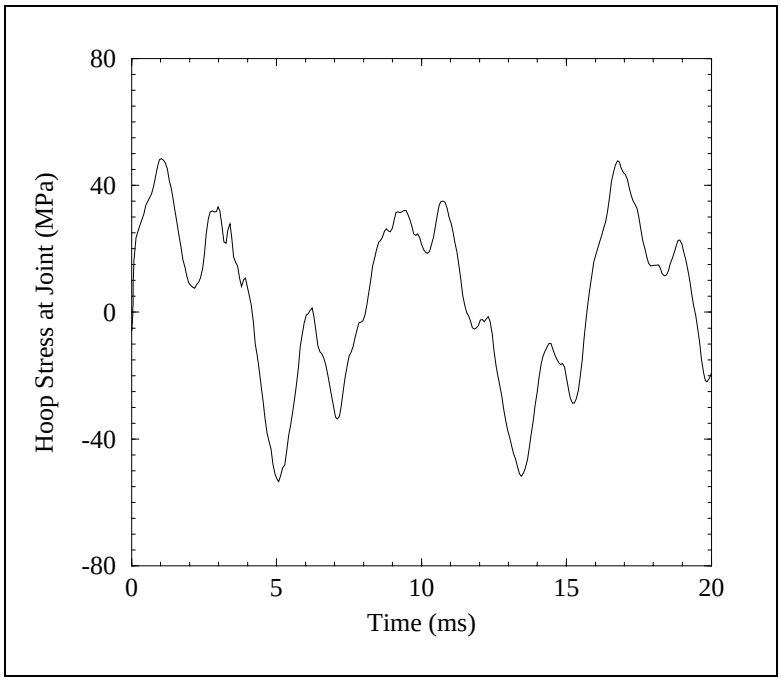

Figure 18. Hoop stress at the junction of the MITLs and the chamber wall from a 40 Pa-s impulse.

3.4 Insulator Stack

There are two options for providing the power to the Z-pinch via the MITLs; they are through an insulator stack and through coaxial tubes. This section pertains to the insulator stack.

The plastic insulator stack option requires an external axial force to hold the plastic stack together by friction. This force should be adequate to keep the vacuum boundary intact against any sudden lateral loading or from buckling from axial loads and/or external pressure. The following is a preliminary study analyzing both of these failure modes.

Mode #1. Elastic stability of thin-walled circular tube under uniform longitudinal compression

r	Radius of tube	= 2.50 m
t	Thickness of tube	= 0.15 m
υ	Poisson's ratio	= 0.4
E	Modulus of elasticity	= 3.06 GPa

Figure 19. An illustration for buckling axial force.

For (r/t) >10, the ends are not constrained.

The formula for critical unit compressive stresses at which elastic buckling occurs is:

$$\sigma' = \frac{E}{\sqrt{3(1-\nu^2)}}\frac{t}{r}$$

Where σ is the critical stress.

Tests indicate an actual buckling strength of 40%-60% of this theoretical value, or (see Warren C. Young)[1]

$$\sigma = 0.3\ Et/r\ .$$

Then:

$$\sigma = 0.3 \times 3.06\times10^{9} \times 0.15/2.5 = 5.4\ \text{MPa}$$

Mode #2. Elastic stability of thin-walled circular tube under uniform radial pressure

r	mean radius of tube	= 2.50 m
t	thickness of tube	= 0.15 m
υ	Poisson's ratio	= 0.4
E	Modulus of elasticity	= 3.06 GPa
I	moment of inertia	= 8.05 m^4

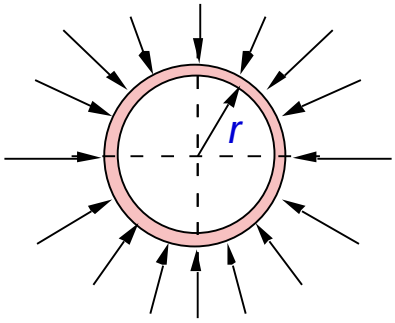

Figure 20. An illustration for buckling radial force.

P' (critical pressure) = $3EI/r^3$

Then:

$$P' = 3 \times 3.06 \times 10^{9} \times 8.05/(2.5)^3 = 4.729\ \text{MPa}$$

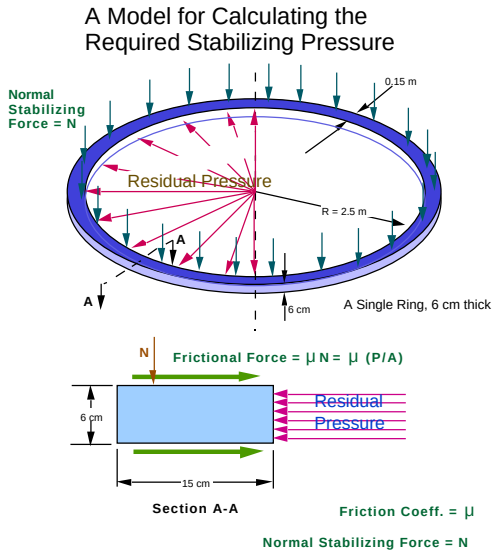

Figure 21. An illustration for static balance between axial force and radial frictional force.

Assumption: Only a single ring would experience the target chamber residual pressure.

A parametric study has been performed to determine the required applied stabilizing pressure to create the radial frictional force to counterbalance the force due to residual pressure. Figure 22 shows the relationship between axial pressure and radial residual pressure.

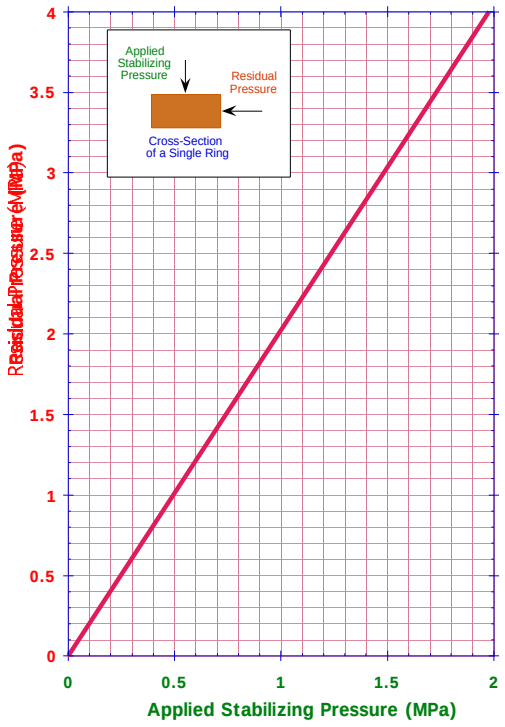

Figure 22. The relationship between axial pressure and radial residual pressure.

Figure 22 shows that the required axial pressure is ≈ 50% of the radial residual pressure assuming a safety factor of 1.0. More appropriately a safety factor of 5 should be used, making the required axial pressure 2.5 times the residual pressure. From the parameter list (Table 2) we find that the residual pressure for a moderate yield shot (200 MJ) is 0.52 MPa and for a high yield shot (1008 MJ) is 3.11 MPa. Using a safety factor of 5 and Figure 22 we find that the needed applied stabilizing pressure is 1.3 MPa and 7.5 MPa for the moderate and high yield shots respectively. The assumption that the residual pressure is applied to only one ring, and a safety factor of 5 are extreme conditions. Nevertheless a pressure of 7.5 MPa (75 atm) can be alleviated substantially by using curved surfaces between the stacks as shown in Figure 23.

Table 2. A parameter list of the residual pressure versus the target yield.

Chamber/Target Parameters/Shots	Units	Moderate	High	No Yield
Target Yield	MJ	200	1008	0
Residual Pressure	MPa	0.52	3.11	0.12

A shallow curvature at the stack ring interfaces would greatly reduce the required axial pressure because of the axial component created due to curvature. The curvature would be optimized to insure the critical electrical and magnetic requirements at the interfaces. Figure 23 shows an illustration of the shallow curvature at the stack ring interfaces.

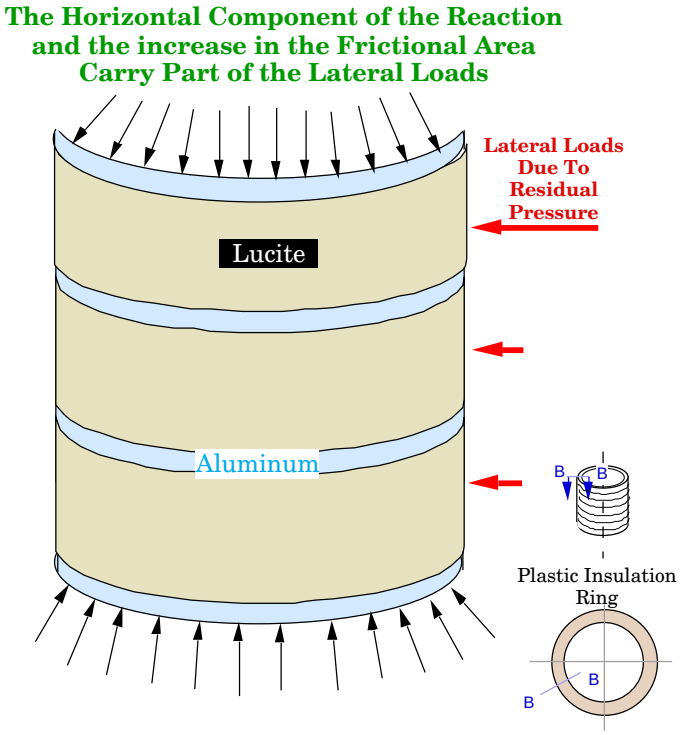

A Longitudinal Cross-Section (B-B) Through Three Rings
Showing a Shallow Curvature in Both Surfaces;
Lucite and Aluminum

Figure 23. An illustration of the shallow curvature at the stack ring interfaces.

3.5 Development Needs

Further analysis of the mechanical response of experiment chamber components is required. The loadings will change as more is learned about the X-1 experimental program and as magnetic debris is further studied. Experiments are required to validate computer codes and analysis methods in the X-1 relevant regimes.

The additional analysis includes:

- Updating of all calculations to reflect changes in target x-ray and debris emission and the full range of X-1 experiments.
- Cratering calculations in the mini-chamber.
- Three-D calculations of the x-ray, debris and vapor flows in the experiment chamber.
- One-D ablation calculations to obtain the vaporization and mechanical loading at various representative positions.
- Three-D finite-element integrated vibration calculations of the mini-chamber, wall and liner, and MITLs.
- Two- or 3-D shock propagation calculations in the mini-chamber.
- Two- or 3-D vapor flow calculations in MITL gaps and the response of insulator stacks to 2 or 3-D loading.
- Fatigue calculations for all permanent components.

Experiments are needed in the following areas:

- Cratering experiments with a gas gun.
- Normal mode tests for all structure types.
- Buckling test for a real flat interface Lucite insulator stack.
- Lateral slip test for a real flat interface Lucite insulator stack under various transverse pressure loads.
- Stability experiments with curved interface Lucite insulator stack.

Reference for Section 3

Warren C. Young, “Roark’s Formulas for Stress and Strain,” 6th edition (McGraw Hill, 1989).

4. Maintenance

Maintenance for the X-1 chamber is very important because it determines to a large extent the availability of the device. For this reason, maintenance should be provided both from the top, and from the bottom of the chamber. In spite of the mini-chamber, the top of the chamber will experience more damage than the bottom because it is close to the explosion and because the bottom part is somewhat shielded by the conical MITLs. The following is a comparison between the top and bottom access maintenance schemes.

From the Bottom	From the Top
Most suitable for yield shots. It could be used for no yield shots.	Most suitable for no yield shots. It could be used for high yield shots.
Decreases the accessibility to the top diagnostics, the mini-chamber, and target zone.	Increases the accessibility to the top diagnostics, mini-chamber, and target zone.
The top liner could be replaced less frequently.	The top liner could be replaced more frequently.
The top water shield stays in place at all times.	The top water shield has to be emptied to a lower level during maintenance.
It takes longer to replace the top dome with diagnostics.	Less time to replace the top dome with diagnostics.
All parts of the chamber are kept under shielding protection at all times during operation and maintenance.	Parts of the chamber are exposed to air without shielding protection during maintenance.

The maintenance concept of dealing with the entire chamber far away from the experimental site after each shot is introduced. With this concept the experimental chamber is to be replaced by a ready-to-go one. To achieve this scheme, all the diagnostic and electrical connections must be disconnected and the water in the lower bottom section must be drained. An elevator would lower the X-1 chamber to an underground arrangement from where it is transferred to a hot cell. In the meantime a ready-to-go X-1 chamber could replace the used one by raising it using the same elevator and making the connections. Figures 24–26 are an illustration of step #1 and step #2 for the top maintenance scheme, top and bottom maintenance scheme, and top assembly scheme.

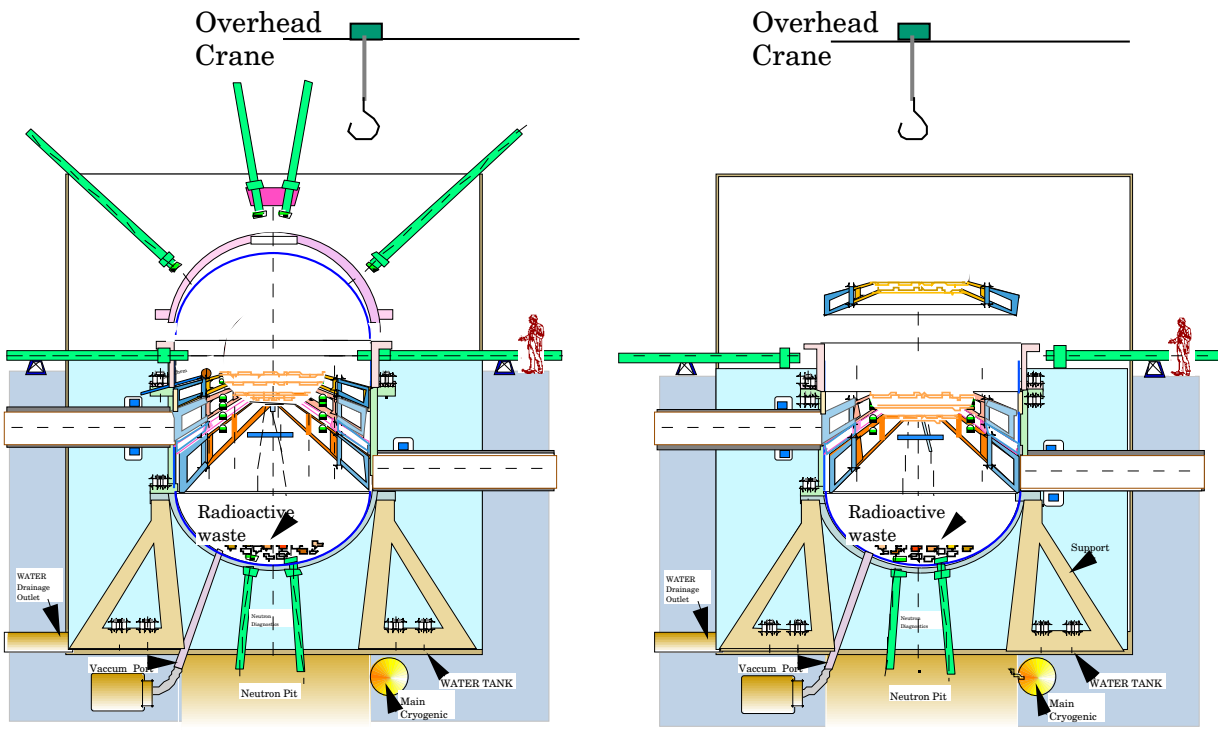

Figure 24. An illustration of step #1 and step #2 for the top maintenance scheme.

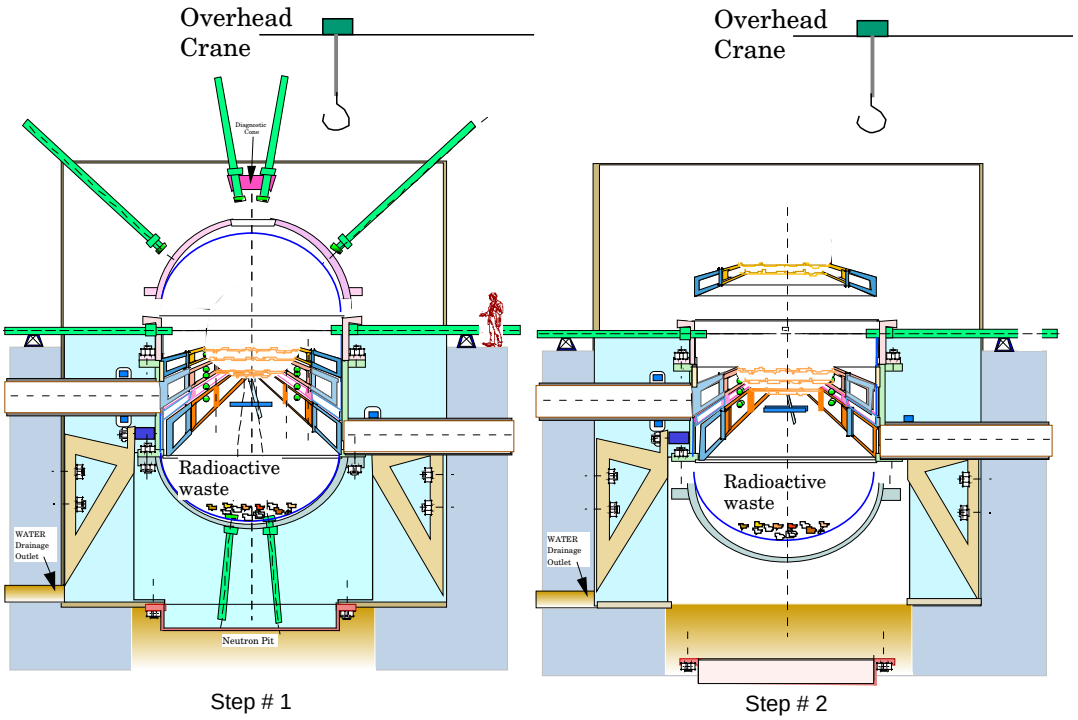

Figure 25. An illustration of step #1 and step #2 for the top/bottom maintenance scheme.

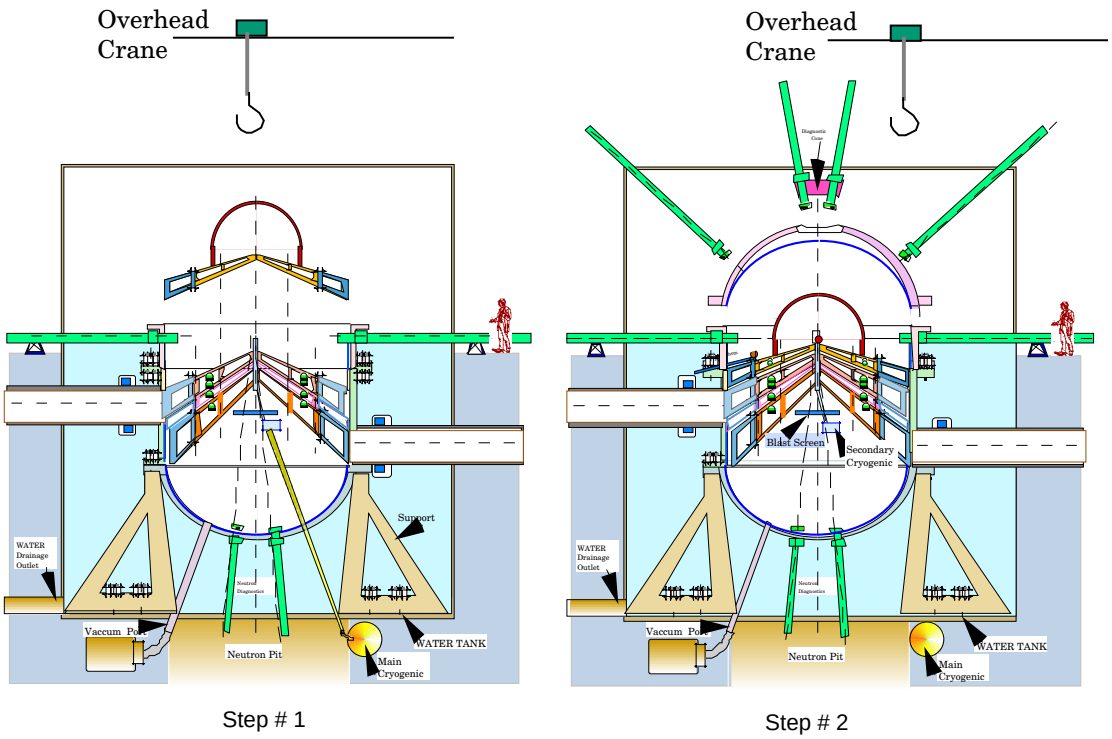

Figure 26. An illustration of step #1 and step #2 for the top assembly scheme.

Critical Issues:

- Survival of the liner of the top part in comparison with the middle and bottom parts.
- Survival of the of the target cryogenic system.

5. Conclusions

A preliminary experiment chamber concept has been completed for X-1 and selected analyses have been made of the chamber. This design is compatible with either the long MITL or water transformer pulsed-power concepts. It is also compatible with target diagnostics and remote removal of the chamber. As the pulsed power and experimental requirements evolve the experimental chamber design will require modification.

Preliminary analysis of the chamber has been performed and there appear to be design solutions for all issues which have arisen thus far. Blast effects, radioactivity and mechanical response have been reported. The general conclusion is that the experimental chamber will need refurbishment after each shot and that after a target explosion with significant fusion yield the operators will not be allowed hands-on access for more than a week. The blast damage is more severe at the highest yields as would be expected. There is clearly an operations price paid for higher thermonuclear yield and this must be considered when the rate of yield shots is determined.

Acknowledgement

Support for this work has been provided by Bechtel Nevada Corp.